nature electronics

Article

https://doi.org/10.1038/s41928-026-01620-5

# Asymmetric thermal transport in a trilayer van der Waals heterostructure

Received: 18 June 2025

Accepted: 29 March 2026

Published online: 05 May 2026

Check for updates

Haidong Wang[1,3] ✉, Hongxin Zhu[1,3], Guodong Xue[2,3], Hongao Yang[1,3], Quanlin Guo[2], Zhike Liu[1], Kaihui Liu[2] ✉ & Bingyang Cao[1] ✉

The heat generated within integrated circuit architectures needs to be efficiently transferred to the package surface through multilayer interfaces in the out-of-plane direction. At the same time, reverse heat flow needs to be blocked to prevent the failure of thermally sensitive components. Achieving the necessary asymmetric phonon transport in the out-of-plane direction is, however, challenging. Here we report a trilayer van der Waals heterostructure that offers asymmetric thermal transport. This thermal Janus crystal is made of molybdenum disulfide ($MoS_2$)/molybdenum sulfide selenide (MoSSe)/tungsten diselenide ($WSe_2$) and has a thickness of less than 5 nm. By precisely adjusting the twist angles at the $MoS_2$/MoSSe and MoSSe/$WSe_2$ interfaces, the asymmetric property—defined as the relative change in the interfacial thermal conductance under opposite temperature gradients—can be tuned from 23% to 104%. Molecular dynamics simulations indicate that the contributions of in-plane and out-of-plane phonon modes at the $MoS_2$/MoSSe and MoSSe/$WSe_2$ interfaces are different, which leads to asymmetry in the heat transport. In a thermal test with a field-effect transistor and using a 58-mW microwire heater, the surface temperature is reduced by 3.9 K when heat flows from $WSe_2$ to $MoS_2$ compared with when the heat flows in the opposite direction through the heterostructure.

In three-dimensional integrated circuits, heat is primarily conducted through multiple interfaces in the out-of-plane direction from internal high-electron-mobility transistors to the external packaging. Effective thermal management, thus, requires efficient heat conduction from the interior to the exterior and blocking reverse heat flow to protect heat-sensitive components. However, achieving nanoscale control of interfacial thermal conductivity and out-of-plane asymmetric phonon transport remains challenging. Thermal rectifiers based on Tesla valve structures, nanopores/nanoparticles and metamaterials[1–5] have been developed. However, these devices typically range in size from tens to hundreds of micrometres and are limited to manipulating heat flow only in the in-plane direction.

Janus crystals—material systems that exhibit different properties on two opposing sides or surfaces[6–13]—could provide a solution to overcome the limitations of size and direction in thermal management technology. Molybdenum sulfide selenide (MoSSe) is a recently developed two-dimensional (2D) Janus material that offers symmetry breaking in three atomic layers and exhibits a giant nonlinear optical response and an anomalous photovoltaic effect[14–16]. However, the thickness of a MoSSe monolayer is far smaller than the phonon mean free path—the average distance a phonon can travel before being scattered—which restricts the control of perpendicular phonon transport across the monolayer.

In this Article, we report a thermal Janus crystal made of molybdenum disulfide ($MoS_2$)/molybdenum sulfide selenide (MoSSe)/tungsten

[1]Department of Engineering Mechanics, Key Laboratory for Thermal Science and Power Engineering of Ministry of Education, Tsinghua University, Beijing, China. [2]State Key Laboratory for Mesoscopic Physics, Frontiers Science Center for Nano-optoelectronics, School of Physics, Peking University, Beijing, China. [3]These authors contributed equally: Haidong Wang, Hongxin Zhu, Guodong Xue, Hongao Yang. ✉e-mail: hdwang@tsinghua.edu.cn; khliu@pku.edu.cn; caoby@tsinghua.edu.cn

diselenide ($WSe_2$) trilayer van der Waals heterostructure, which is inspired by the control of electronic energy band and correlated states in magic-angle 2D dimensional materials with moiré superlattices[17–26]. By finely tuning the twist angles at the $MoS_2$/MoSSe and MoSSe/$WSe_2$ interfaces, the spacing between adjacent atoms on both sides of MoSSe and the interlayer van der Waals force can be modulated[27,28], enhancing control over phonon transport.

The asymmetric thermal transport property ($\eta$) is quantified as the relative change of thermal conductance ($G$) in the opposite temperature gradient directions. We develop an X-shaped sensor to measure the thermal conductance in different vertical heat flow directions. By independently changing the twist angles at the $MoS_2$/MoSSe and MoSSe/$WSe_2$ heterointerfaces, $\eta$ can be tuned from 23% to 104%. Molecular dynamics simulations show that the contributions of in-plane and out-of-plane phonon modes to the interfacial thermal conductance at two interfaces are different, which results in asymmetric phonon transport. We measure the surface temperature of the trilayer material placed on a microwire heater by using a thermoreflectance thermal imaging (TTI) method. The measured surface temperature is 3.9 K lower when heat flows from $WSe_2$ to $MoS_2$ than when it flows in the opposite direction at an input power of 58 mW.

## Fabrication of X-shaped sensors

To measure the forward and reverse out-of-plane thermal conductance of the $MoS_2$/MoSSe/$WSe_2$ trilayer heterostructure, we designed and fabricated X-shaped sensors (Fig. 1). First, a bottom gold nanosensor (1 μm × 15 μm, 50 nm thick) was deposited onto a $SiO_2$/Si substrate through physical vapour deposition (PVD) (Fig. 1a). Subsequently, three triangular single-crystalline transition-metal dichalcogenide (TMD) monolayers ($MoS_2$, MoSSe and $WSe_2$) were mechanically transferred with precisely controlled twist angles $\theta_1$ and $\theta_2$ (Methods provides details on Janus MoSSe fabrication). The transfer process of a triangular TMD monolayer involved the following. (1) A polymethyl methacrylate (PMMA) film was spin coated on top of a single-crystalline $MoS_2$ monolayer substrate. (2) Using the microknife (MKS-15) equipped on the micromanipulation system, a single-crystalline $MoS_2$ triangular domain supported by PMMA was cut off and removed from the substrate. (3) A pair of microprobes were used to mechanically transfer the monolayer $MoS_2$ crystal domain onto the target surface. Both position and orientation of the triangular crystal domain were meticulously adjusted. To precisely control the twist angle, one corner of the PMMA film was anchored by probe A, whereas probe B was used to nudge the opposite corner and turn the sample to the desired twist angle (Fig. 1k; Supplementary Video 1 provides details). (4) The PMMA layer was removed through immersion into warm butanone. Annealing at 400 °C for 8 h was conducted to eliminate possible contaminations or residues on the sample. The same procedure was repeated to transfer MoSSe and $WSe_2$ (Methods).

The other gold nanosensor perpendicular to the bottom sensor was deposited on top of the trilayer TMD sample, creating an Au/$MoS_2$/MoSSe/$WSe_2$/Au stack from bottom to top (Fig. 1e,j). In particular, a 3 μm × 3 μm × 50 nm $SiO_2$ square was fabricated at the centre of the X-shaped sensors to support the $MoS_2$/MoSSe/$WSe_2$ trilayer. The remaining TMD materials outside the square were etched away. The whole X-shaped sensors were fully suspended from the substrate by using $XeF_2$ gas etching (Fig. 1o,p), to achieve the highest possible thermal measurement sensitivity.

To further evaluate the quality of interface between stacked TMD layers, the aberration-corrected transmission electron microscopy (TEM) was used to examine the cross-sectional view of the trilayer heterostructure (Fig. 1n). The images revealed the good flatness and cleanliness of the heterogeneous interfaces. The interlayer distance between $MoS_2$ and MoSSe and that between MoSSe and $WSe_2$ were measured to be 0.68 nm and 0.67 nm, respectively, aligning with the theoretical expectation of 0.65 nm (ref. 27). This result demonstrates the good quality of the heterointerface achieved through the used mechanical transfer technology. In particular, the current method used to transfer monolayer TMD single-crystal domain is generalizable and can be applied to transfer and stack various 2D materials. Using this approach, we have fabricated different stacked structures for comparison, like Au/$MoS_2$/Au, Au/$MoS_2$/$MoS_2$/Au and Au/$MoSe_2$/$WSe_2$/Au.

## Atomic-scale stacking characterization

For the $MoS_2$/$MoS_2$ and $MoSe_2$/$WSe_2$ heterostructures, the twist angle between the two layers of 2D materials was defined as $\theta$ (Fig. 2a), representing the average angle of the corresponding edges of the top and bottom triangles. This angle was measured using optical microscopy (OM) with an error of approximately 0.3° (Supplementary Section 3). For the $MoS_2$/MoSSe/$WSe_2$ trilayer heterostructure samples, we used MoSSe as the benchmark and recorded the twist angle between MoSSe and $MoS_2$ and that between MoSSe and $WSe_2$ as $\theta_1$ and $\theta_2$, respectively (Fig. 1l). To assess the precision of the twist angle measurements obtained from OM, the polarization-resolved second-harmonic generation (SHG) spectra were used to determine the lattice orientation of the bilayer twisted $MoS_2$ (Fig. 2b–d). In the non-overlapping regions of the upper and lower layers of $MoS_2$, the SHG signal exhibits distinct six-fold rotational symmetry, attributable to the three-fold rotational symmetry of the $MoS_2$ lattice. The directions of the maximum SHG signal intensity correspond to the armchair crystallographic directions. Consequently, the twist angles could be extracted by fitting the SHG patterns as 0.09°, 14.23° and 29.18° in Fig. 2e–g, respectively, which is consistent with the corresponding values of 0.1°, 14.5° and 29.6° obtained through the OM measurements. This agreement demonstrates the reliability of the angular measurements in our mechanical transfer technology.

Furthermore, we examined the overlapping region of $MoS_2$ using scanning TEM. The atomically resolved moiré patterns presented in Fig. 2h–j confirm the high crystallinity and exceptional transfer efficacy of TMD. The moiré fringe periodicity in twisted bilayer $MoS_2$ can be computed as follows:

$$L = \frac{a}{\sqrt{2(1-\cos\theta)}}, \quad (1)$$

where $L$ is the moiré length and $a$ represents the lattice constant of $MoS_2$, which is 0.3125 nm. $\theta$ denotes the twist angle. The measured moiré periodicities (Fig. 2h–j) are 2.79 nm, 1.47 nm and 0.64 nm, respectively, corresponding to theoretical twist angles of 6.4°, 12.2° and 28.5°. The Raman mappings were also performed for the MoSSe, $MoS_2$, $WSe_2$ and $MoSe_2$ monolayers (Fig. 2k), which indicated the large-area uniformity of the samples. Their characteristic peak positions of the $A_{1g}$ modes for the four samples were located at 290.5 $cm^{-1}$, 406.5 $cm^{-1}$, 260.1 $cm^{-1}$ and 241.3 $cm^{-1}$, respectively, whereas the corresponding $E_{2g}$ mode characteristic peak positions were observed at 358.6 $cm^{-1}$, 384.6 $cm^{-1}$, 250.8 $cm^{-1}$ and 292.6 $cm^{-1}$, consistent with the data reported in the existing literature[28–32] (Supplementary Fig. 2). Although $MoSe_2$/$WSe_2$ and $MoS_2$/MoSSe/$WSe_2$ heterostructures exhibited similar colours in the OM images, the distinct Raman peak characteristics confirmed their layer-by-layer stacking configurations, consistent with our cross-sectional aberration-corrected TEM results (Fig. 1n).

## Out-of-plane thermal conductance measurement and asymmetry heat transport characteristics

Using the X-shaped sensor approach, we measured the out-of-plane thermal conductance $G$ of all the $MoS_2$/$MoS_2$, $MoSe_2$/$WSe_2$ and $MoS_2$/MoSSe/$WSe_2$ heterostructures under different heat flow directions, similar to the H-type sensor for measuring the in-plane thermal conductivity in our previous work[33]. In this setup, the bottom and top sensors of the suspended device functioned as a 'Joule heater' and a precise 'resistance thermometer', respectively. The role of the heater

https://doi.org/10.1038/s41928-026-01620-5

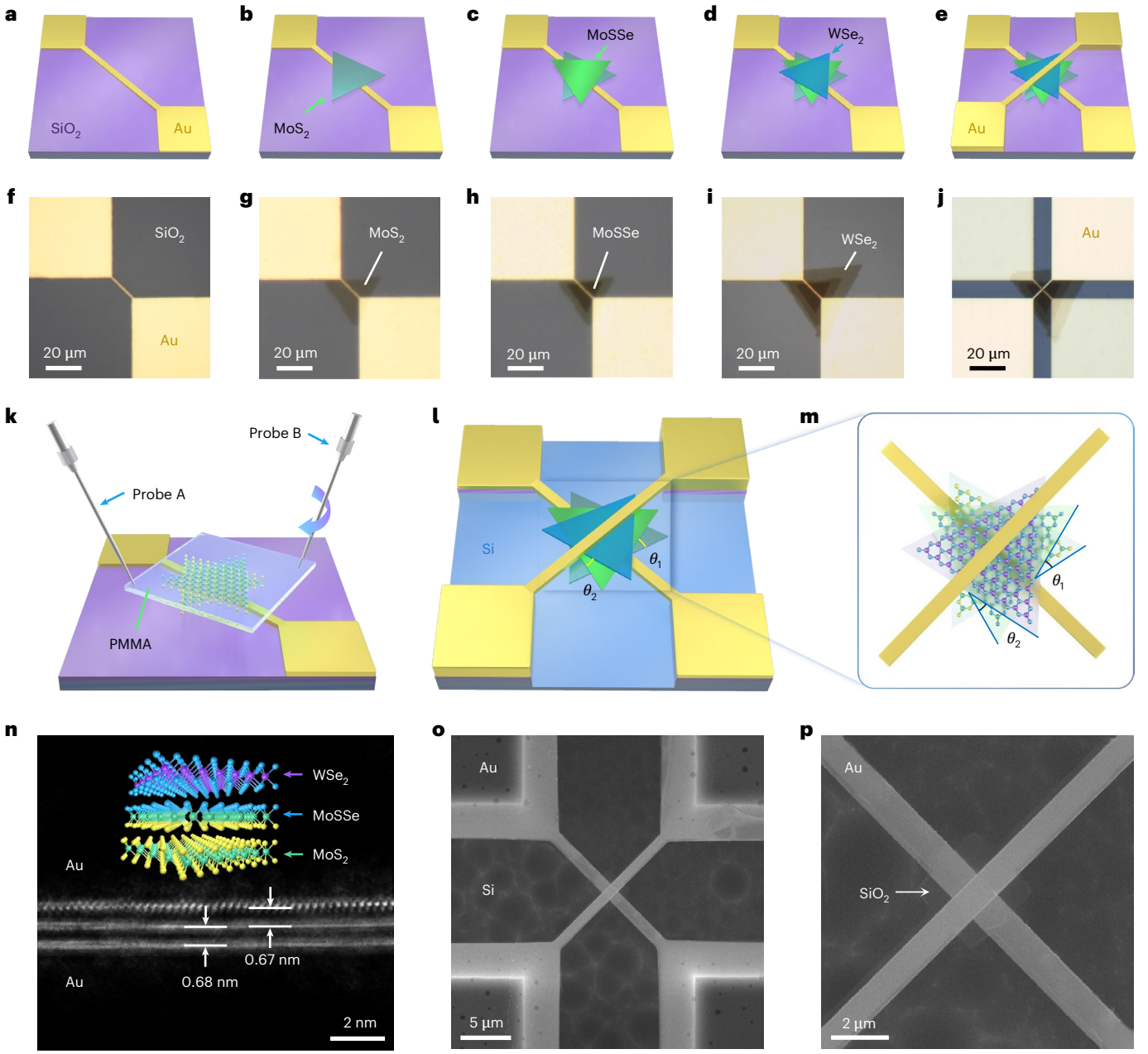


**Fig. 1 | Fabrication of X-shaped sensors for measuring the out-of-plane thermal conductance of trilayer $MoS_2$/MoSSe/$WSe_2$ heterostructure.** **a**, Deposition of the bottom gold nanosensor onto the $SiO_2$/Si substrate through PVD. **b**, Mechanical transfer of a triangular single-crystalline $MoS_2$ monolayer onto the bottom sensor. **c**, Mechanical transfer of a triangular single-crystalline Janus MoSSe monolayer onto $MoS_2$ with a twist angle $\theta_1$. **d**, Mechanical transfer of a triangular single-crystalline $WSe_2$ monolayer onto MoSSe with a twist angle $\theta_2$. **e**, Deposition of the top gold nanosensor onto $WSe_2$ through PVD. **f**–**j**, OM images from steps shown in **a**–**e** (**f**–**j**, respectively). **k**, Precise control of $\theta_1$ and $\theta_2$ between two neighbouring TMD monolayers by using a pair of microprobes. **l**, Etch the $SiO_2$ layer and exposed Si substrate by using reactive ion etching and $XeF_2$ gas, respectively, to suspend the X-shaped sensors together with a trilayer sample in between. **m**, Schematic of the core structure in the middle of the X-shaped sensors. **n**, Aberration-corrected TEM image of the cross-section of the Au/$MoS_2$/MoSSe/$WSe_2$/Au stacking layers. **o**,**p**, SEM images of suspended X-shaped sensors with trilayer TMD samples supported by a 3 μm × 3 μm × 50 nm $SiO_2$ square.

and thermometer can be switched by simply changing the electrical current through each independent sensor, allowing the heat flow direction to be reversed (Fig. 3a). For a constant heating power, higher out-of-plane thermal conductance results in a greater temperature rise in the thermometer sensor. Using the measured heating power and temperature rises as input, the thermal conductance can be calculated via three-dimensional thermal simulations of the heat conduction equation (Methods). Before thermal measurement, the out-of-plane electrical transport properties of all heterostructure samples were measured. The drain–source current–voltage ($I_{ds}$–$V_{ds}$) curve (Fig. 3b) indicated no appreciable electrical rectification, probably because of the narrow depletion layer within the heterojunction, which was only several atoms thick and, thus, did not generate a sufficient built-in electric field[34]. Moreover, when $V_{ds}$ was below 0.2 V, the interfacial resistance for all heterostructures remained above 150 Ω, substantially higher than the resistance of the gold sensor (approximately 15.6 Ω). This confirms no direct contact between the top and bottom sensors and no electrical breakdown within the heterostructure. Extreme electrical tests on the Au/$MoS_2$/Au stacked structure (Supplementary Fig. 3) revealed that the resistance between two sensors was maintained stable above

https://doi.org/10.1038/s41928-026-01620-5

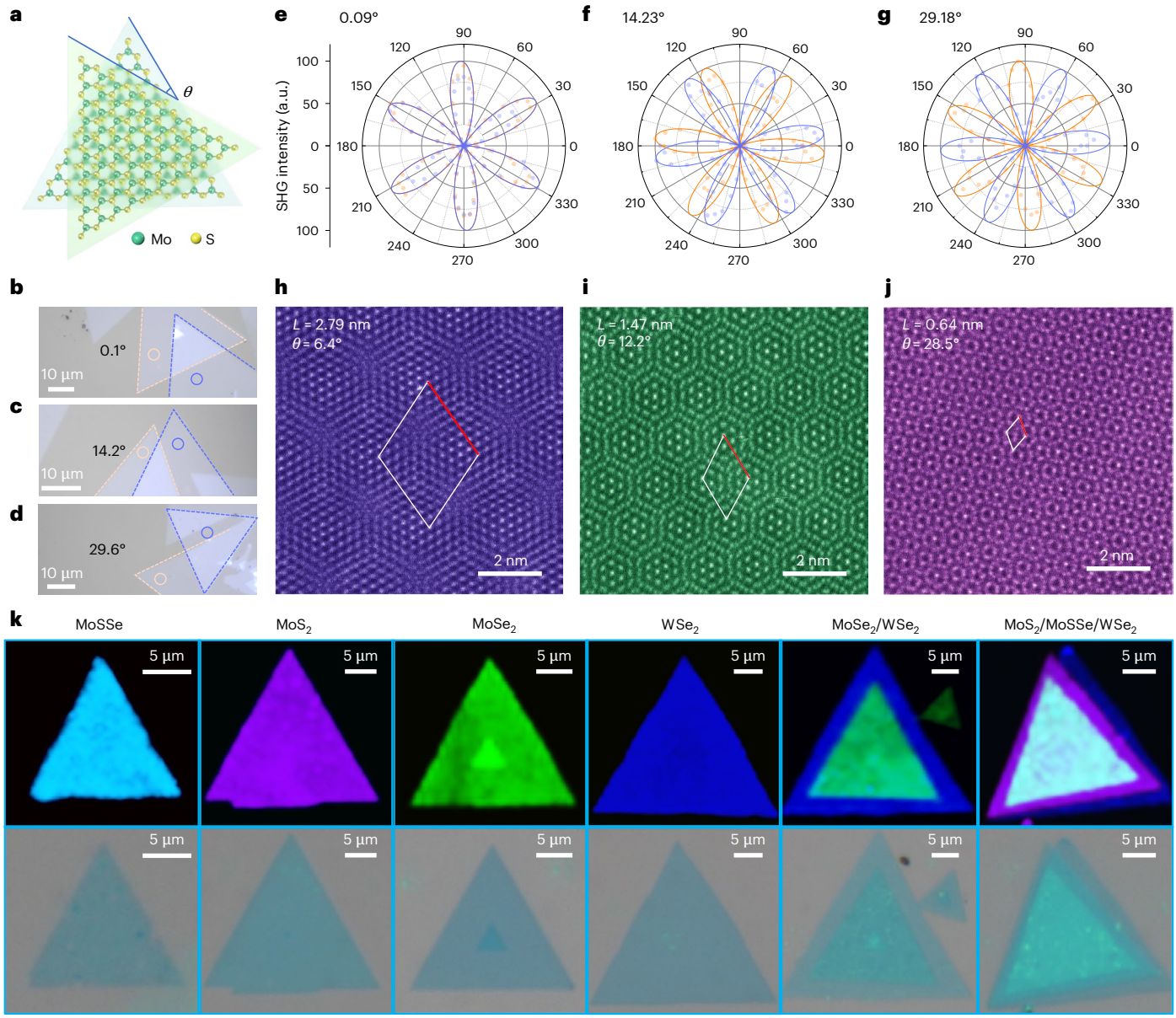


**Fig. 2 | Accurate characterization of the twist angle and moiré patterns in twisted heterostructures. a**, Schematic of $\theta$ for the $MoS_2/MoS_2$ bilayer. **b**–**d**, OM images of three triangular $MoS_2/MoS_2$ bilayer samples and the angle measurement results. **e**–**g**, Polarization-resolved SHG characterization results corresponding to the regions shown in **b**–**d** (**e**–**g**, respectively), with the measurement area indicated by the circles in **b**–**d**. **h**–**j**, Scanning TEM images of $MoS_2/MoS_2$ heterostructures with three twist angles. The white rhombuses indicate moiré periodic stripes and the red edges represent the moiré lengths $L$. **k**, Raman spatial mapping images of monolayer MoSSe, $MoS_2$, $MoSe_2$ and $WSe_2$ samples, as well as $MoSe_2/WSe_2$ and $MoS_2/MoSSe/WSe_2$ heterostructures.

130 Ω within a voltage range below 189 mV (Supplementary Video 2). To avoid electrical breakdown, the voltage applied to the gold sensors in the subsequent measurement of the out-of-plane thermal conductance was below 100 mV. Moreover, detailed circuit analysis further confirms the absence of leakage current during thermal measurements (Supplementary Fig. 5), precluding Joule heating arising from contact resistance and ensuring measurement reliability.

All the thermal measurements were conducted in a high-vacuum chamber (pressure, $<10^{-3}$ Pa) to avoid convective heat loss. The radiative heat transfer can be neglected, too (Supplementary Section 3). The overlapping region between the top and bottom sensors was only 1 μm × 1 μm, that is, the same region in which the heterostructure sample was positioned, much smaller than the area of the sensor (15 μm × 1 μm). Therefore, the surface temperature distribution within the overlapping region was essentially uniform (within 0.15 K, as confirmed by a finite element simulation). Consequently, heat transfer predominantly occurred in the out-of-plane direction across the heterostructure and could be modelled using a one-dimensional thermal resistance network. In general, the total thermal resistance, $1/G_{eff}$, includes the interfacial thermal resistance $1/G_s$ between Au and TMD and $1/G$ between TMD layers:

$$1/G_{eff} = 1/G_s + 1/G. \quad (2)$$

The calibration of $G_s$ was conducted using three specifically designed stacked structures: Au/$MoS_2$/Au, Au/$MoSe_2$/Au and Au/$WSe_2$/Au. A comprehensive description of the calibration methodology is provided in Supplementary Section 1. At the ambient temperature (293 K), the measured values are as follows: $G_{Au/MoS_2}$ is 28.48 ± 2.28 MW m$^{-2}$ K$^{-1}$, $G_{Au/MoSe_2}$ is 33.92 ± 2.72 MW m$^{-2}$ K$^{-1}$ and $G_{Au/WSe_2}$ is

https://doi.org/10.1038/s41928-026-01620-5

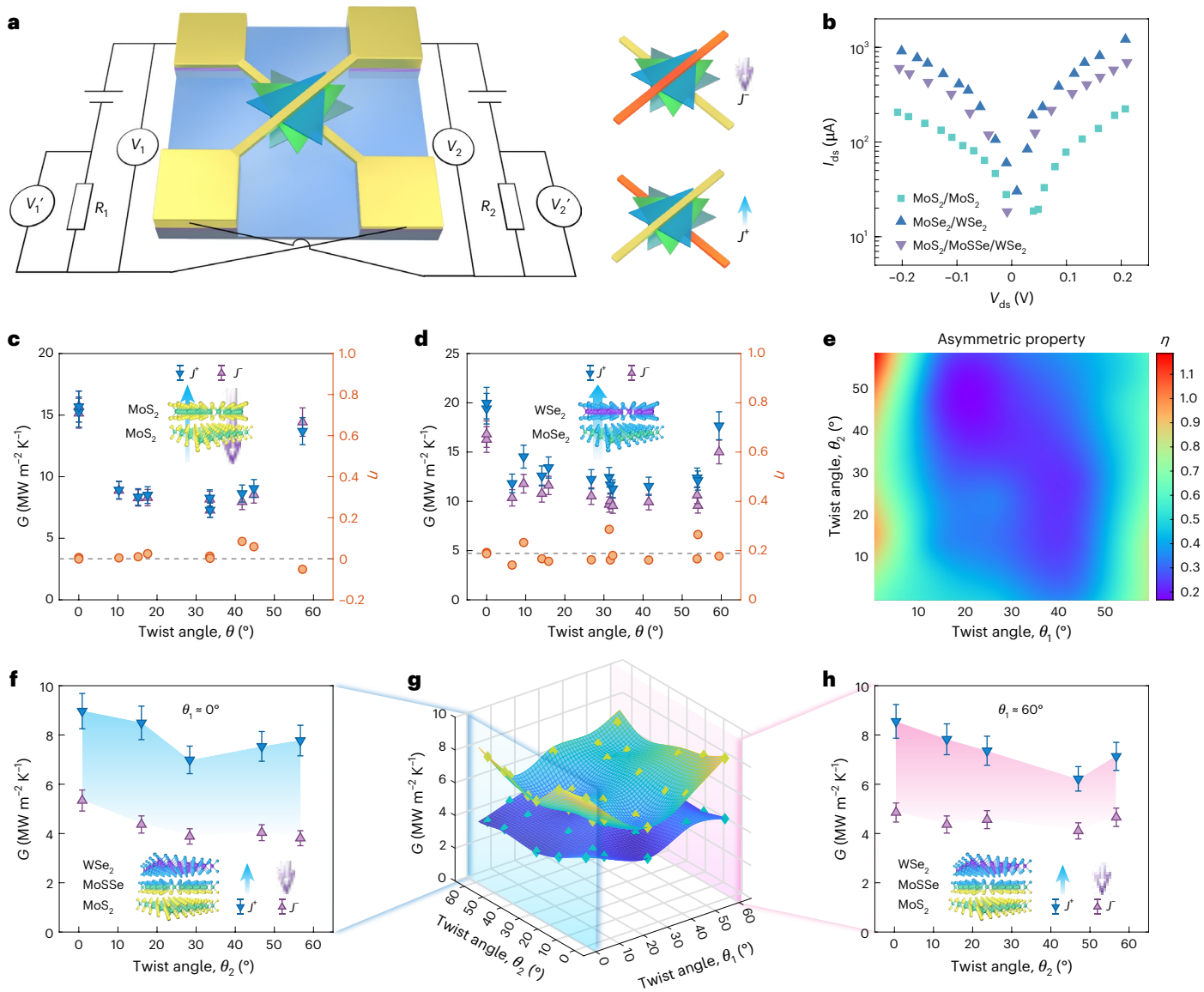


**Fig. 3 | Out-of-plane thermal conductance measurement circuit and the asymmetry heat transport characteristics of $MoS_2/MoS_2$, $MoSe_2/WSe_2$ and $MoS_2/MoSSe/WSe_2$ heterostructures. a**, Schematic of the electrical circuit for measuring the out-of-plane thermal conductance using the X-shaped sensors. $V_1$ and $V_2$ measure the voltage of the bottom and top sensors, respectively. $V_1'$ and $V_2'$ correspondingly measure the electrical current in each loop. The blue solid arrow indicates the heat flow direction $J^+$ from the bottom to the top sensor, and the purple hollow arrow indicates the heat flow direction $J^-$ from the top to the bottom sensor. **b**, $I_{ds}$–$V_{ds}$ characterization in the out-of-plane direction of bilayer $MoS_2/MoS_2$, $MoSe_2/WSe_2$ and trilayer $MoS_2/MoSSe/WSe_2$ heterostructures. **c**,**d**, Variations in the out-of-plane thermal conductance of bilayer $MoS_2/MoS_2$ (**c**) and $MoSe_2/WSe$ (**d**) heterostructures in two opposite heat flow directions with $\theta$, respectively. **e**, Variations in $\eta$ of trilayer $MoS_2/MoSSe/WSe_2$ heterostructure with twist angles $\theta_1$ and $\theta_2$. **g**, Variations in the out-of-plane thermal conductance of trilayer $MoS_2/MoSSe/WSe_2$ heterostructure in two opposite heat flow directions with $\theta_1$ and $\theta_2$. **f**,**h**, Variations in thermal conductance with $\theta_2$ for $\theta_1 \approx 0°$ and $\theta_1 \approx 60°$, respectively. The shaded area highlights the difference in interfacial thermal conductance under $J^+$ and $J^-$ heat flow conditions. Each data point in **c**, **d**, **f** and **h** represents an independent measurement result for a single sample. The vertical lines at each data point indicate a combined standard uncertainty of ±8%. A detailed calculation of the uncertainty can be found in Supplementary Section 3.

21.16 ± 1.70 MW m$^{-2}$ K$^{-1}$, consistent with the values reported in other studies[35–38], confirming the reliability of the X-shaped sensor measurement approach.

By subtracting $G_s$ from $G_{eff}$, the interfacial thermal conductance $G$ between $MoS_2/MoS_2$ layers was determined as a function of $\theta$ (Fig. 3c). The dependence of $G$ on the twist angle was symmetric around $\theta = 30°$, consistent with the three-fold rotational symmetry of the $MoS_2$ crystal. The effective range of the twist angle was 0°–30° (ref. 28). Within this range, $G$ reached its maximum value of 15.7 MW m$^{-2}$ K$^{-1}$ at $\theta = 0.3°$, after which it rapidly decreased with an increase in the twist angle. Conversely, from 10° to 30°, $G$ remained almost unchanged, consistent with prior experimental results by time-domain thermoreflectance and micro-Raman methods[28,39,40]. The thermal conductance across the interface showed minimal variation with different heat flow directions. The asymmetric property of heat transfer ($\eta$) is equal to the ratio of $G$ in two opposite heat flow directions minus one ($\eta = G^+/G^- - 1$). $\eta$ remained consistently below 3% at the most investigated angle, indicating no asymmetry of heat transport effect, aligning with theoretical predictions. For the $MoSe_2/WSe_2$ heterostructure, the variation in $G$ with twist angle was consistent with that of the $MoS_2/MoS_2$ heterostructure (Fig. 3d). In the heat flow direction from $MoSe_2$ to $WSe_2$ ($J^+$ direction), the interfacial thermal conductance $G$ at 14 different angles were all

https://doi.org/10.1038/s41928-026-01620-5

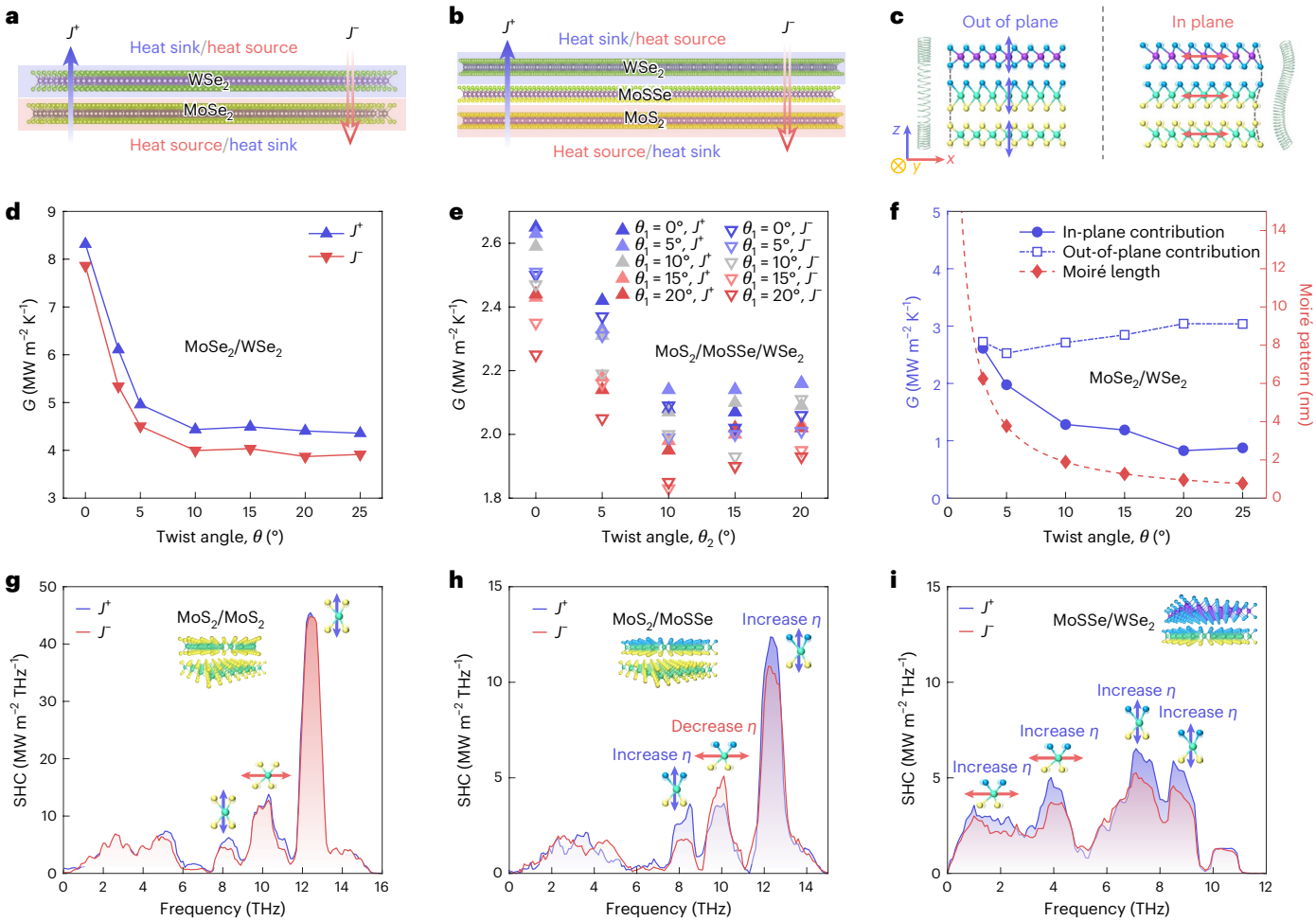


**Fig. 4 | Non-equilibrium molecular dynamics simulations revealing the physical mechanisms of asymmetry of heat transport. a**,**b**, Schematic of the $MoSe_2/WSe_2$ (**a**) and $MoS_2/MoSSe/WSe_2$ (**b**) heterostructure models. **c**, Schematic of the contributions of the in-plane and out-of-plane phonon modes to the out-of-plane heat transfer. **d**,**e**, Variation in the interfacial thermal conductance of the $MoSe_2/WSe_2$ (**d**) and $MoS_2/MoSSe/WSe_2$ (**e**) heterostructures with the twist angle in both $J^+$ and $J^-$ heat flow directions, respectively. **f**, Contributions of in-plane and out-of-plane phonon modes to the interfacial thermal conductance of the $MoSe_2/WSe_2$ heterostructure. **g**–**i**, SHC decomposition of the interfacial thermal conductance of the $MoS_2/MoS_2$ homointerface (**g**), $MoS_2/MoSSe$ heterointerface (**h**) and $MoSSe/WSe_2$ heterointerface (**i**). The shaded region serves to highlight the difference in SHC between $J^+$ and $J^-$ heat flow conditions.

higher than that in the opposite direction ($J^-$ direction), and the maximum value of $\eta$ reached up to 29%. However, $\eta$ showed no apparent angular dependence in the $MoSe_2/WSe_2$ heterostructure, with its value fluctuating around an average of 19%.

The incorporation of the Janus MoSSe monolayer between $MoS_2$ and $WSe_2$ further enhanced the asymmetry of the molecular structure vertically and increased the asymmetry of heat transport. The out-of-plane thermal conductance $G$ of 25 $MoS_2/MoSSe/WSe_2$ trilayer heterostructures were measured at different angles of $\theta_1$ and $\theta_2$ (Fig. 3g). For clarity, the variation in $G$ with $\theta_2$ was extracted at $\theta_1 \approx 0°$ and $\theta_1 \approx 60°$ (Fig. 3f,h, respectively). Evidently, $G$ reached its maximum value when both $\theta_1$ and $\theta_2$ approach 0°, consistent with the measurement results of the $MoS_2/MoS_2$ and $MoSe_2/WSe_2$ bilayer heterostructures. Figure 3e represents a graphical result of the correlation between $\eta$ and the angles $\theta_1$ and $\theta_2$. In the heat flow direction from $MoS_2$ to $WSe_2$ ($J^+$ direction), the out-of-plane thermal conductance $G$ of all 25 samples with different angles was higher than that in the opposite direction ($J^-$ direction), with the maximum $\eta$ reaching 104%. Remarkably, the angular orientation was found to play a pivotal role in the modulation of $\eta$. Specifically, $\eta$ could be effectively modulated by varying the twist angle, with values ranging from 23% (at $\theta_1 = 30.0°$, $\theta_2 = 46.9°$) to 104% (at $\theta_1 = 2.2°$, $\theta_2 = 56.6°$).

## Physical mechanisms underlying asymmetry of heat transport

We have conducted non-equilibrium molecular dynamics simulations to elucidate the physical mechanisms of the asymmetry of heat transport. In twisted bilayer $MoS_2$, $MoSe_2/WSe_2$ and twisted trilayer $MoS_2/MoSSe/WSe_2$ simulation models, the temperatures of the top and bottom layers were controlled by using Langevin heat baths to induce the vertical temperature gradient (Fig. 4a,b). The simulation results indicated the absence of the asymmetry of heat transport in the twisted bilayer $MoS_2$ (Supplementary Section 2), as expected due to molecular symmetry. In twisted $MoSe_2/WSe_2$, heat preferentially flowed from $MoSe_2$ to $WSe_2$ (Fig. 4d). The interfacial thermal conductance decreased with increasing twist angle, consistent with the experimental results. In twisted trilayer $MoS_2/MoSSe/WSe_2$, heat predominantly flowed from $MoS_2$ to $WSe_2$ (Fig. 4e), and the increasing twist angles $\theta_1$ and $\theta_2$ led to the reduced out-of-plane thermal conductance. Phonon density of states (DOS) overlap is often used to reflect the matching of phonon spectra between two materials, qualitatively characterizing the relative magnitude of interfacial thermal conductance. In twisted $MoSe_2/WSe_2$, the calculated DOS overlap of the Se atoms closest to the interface was higher when heat flowed from $MoS_2$ to $WSe_2$, reflecting the vertical asymmetry of heat transport behaviour (Supplementary Fig. 11).

https://doi.org/10.1038/s41928-026-01620-5

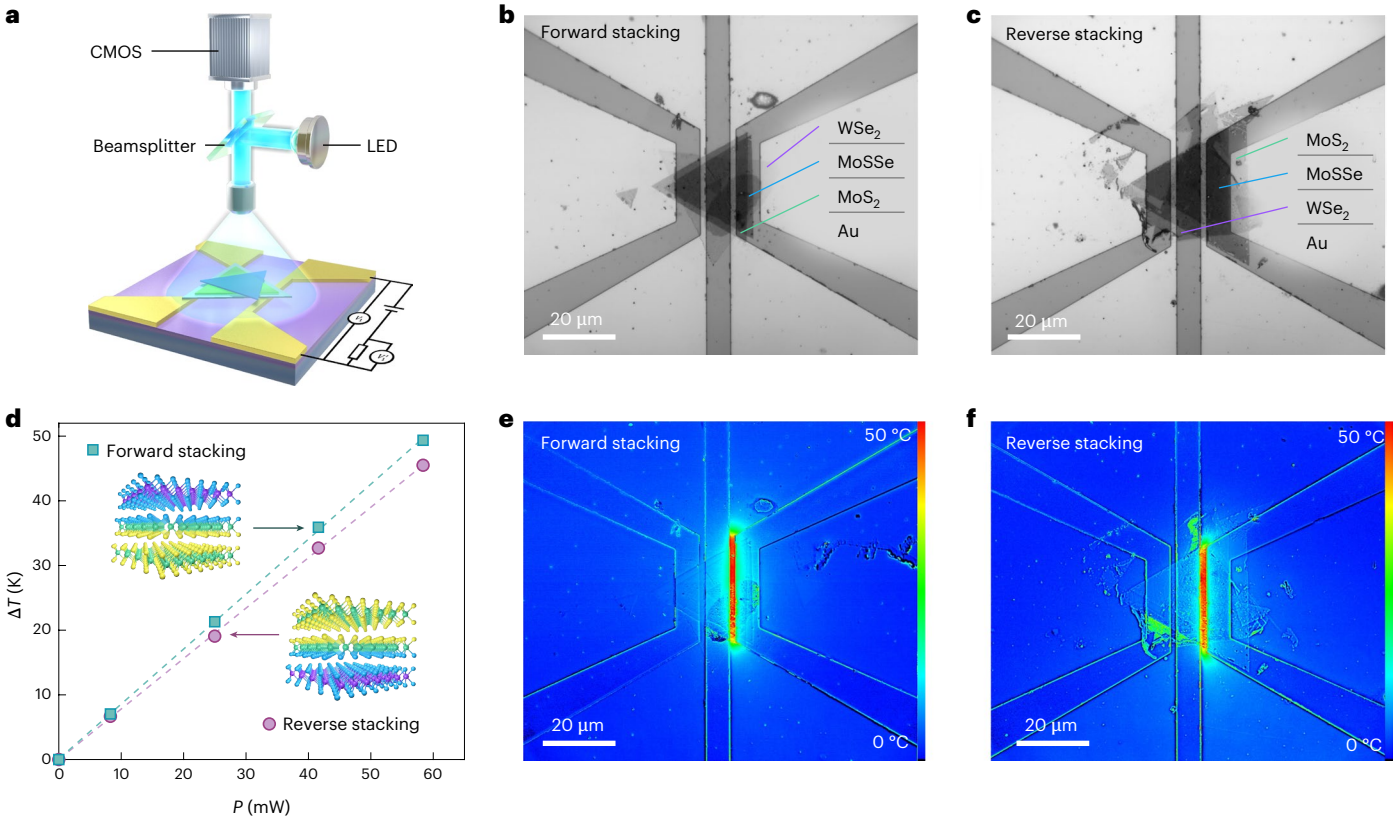


**Fig. 5 | Validation of the asymmetry of heat transport effect in FET devices by using the TTI system. a**, Schematic of the TTI system to measure the surface temperature distribution of the device. The thin gold electrode acts as a Joule heater under the $MoS_2$/MoSSe/$WSe_2$ trilayer heterostructure. CMOS, complementary metal–oxide–semiconductor; LED, light-emitting diode. **b**, OM image of the forward-stacked heterostructure on the electrode (Au/$MoS_2$/MoSSe/$WSe_2$ from bottom to top). **c**, OM image of the reverse-stacked heterostructure on the electrode (Au/$WSe_2$/MoSSe/$MoS_2$ from bottom to top). **d**, Surface temperature of the trilayer material directly above the gold electrodes as a function of heating power. **e**,**f**, Temperature distributions of the structures in **b** (**e**) and **c** (**f**) at a heating power of 58 mW.

We have performed spectral heat current (SHC) decomposition to differentiate the contributions of phonons at different frequencies and different vibration modes. The in-plane phonon modes, which are contributed by the movement of atoms in the *x* or *y* direction, manifest as transverse waves in the interfacial heat conduction. Conversely, the out-of-plane phonon modes, resulting from the movement of atoms in the *z* direction, appear as longitudinal waves in the interfacial heat conduction (Fig. 4c). For the $MoSe_2$/$WSe_2$ heterostructure shown in Fig. 4f, with an increasing twist angle, the in-plane component of the interfacial thermal conductance decreased substantially, whereas the out-of-plane component increased slightly. This could be attributed to the reduction in the moiré pattern length *L* with increasing twist angle, which, in turn, suppresses the transport of long-wavelength phonons. Further frequency-domain decomposition of the SHC confirms this finding. With the increasing twist angle, the low-frequency component of the in-plane SHC decreased, whereas the high-frequency component of the out-of-plane SHC increased (Supplementary Fig. 13). This indicates that larger moiré patterns, characterized by longer periodicity, facilitate the coupling of long-wavelength, low-frequency in-plane phonons. Conversely, smaller moiré patterns, with shorter periodicity, enhance the coupling strength of short-wavelength, high-frequency out-of-plane phonons. Similar results were observed at two interfaces in twisted trilayer $MoS_2$/MoSSe/$WSe_2$, explaining the dependence of interfacial thermal conductance on twist angle.

To further elucidate the asymmetry of the heat transport mechanism, we meticulously investigated the SHC at the interfaces in different heat flow directions. For the $MoS_2$/$MoS_2$ homointerface, the SHC profiles in both $J^+$ and $J^-$ heat flow directions are essentially coincident (Fig. 4g), indicating the absence of asymmetry of heat transport effects, as expected. By contrast, we calculated the trilayer $MoS_2$/MoSSe/$WSe_2$ heterostructure and extracted the SHC curves for its constituent $MoS_2$/MoSSe and MoSSe/$WSe_2$ heterointerfaces. These curves exhibit substantial differences in the $J^+$ and $J^-$ heat flow directions (Fig. 4h,i): the interfacial thermal conductance at the $MoS_2$/MoSSe interface was predominantly attributed by the high-frequency phonons in the 7–15-THz range, whereas at the MoSSe/$WSe_2$ interface, the contribution of low-frequency phonons (0–5 THz) was approximately equal to that of the high-frequency phonons. This discrepancy demonstrates that the existence of Janus material MoSSe creates notable asymmetric SHC at the two heterointerfaces above and below, which is a key factor to the out-of-plane asymmetry of the heat transport effect. Furthermore, the phonon mode analysis revealed that at the $MoS_2$/MoSSe heterointerface, the contribution of out-of-plane phonons to SHC was larger in the $J^+$ direction than that in the $J^-$ direction, whereas the contribution of in-plane phonons was larger in the $J^-$ direction than that in the $J^+$ direction, suggesting a competitive relationship between different phonon modes on the asymmetry of heat transport (Supplementary Fig. 14). By contrast, at the MoSSe/$WSe_2$ heterointerface, both in-plane and out-of-plane phonons made contributions to the asymmetry of heat transport in the $J^+$ direction and increased the ratio $\eta$. These findings were based on a detailed statistical analysis of 12 different combinations of $\theta_1$ and $\theta_2$ angle configurations (Supplementary Figs. 15–17). Consequently, the pronounced differences in the SHC profiles at the two heterointerfaces, along with the distinct contributions from the in-plane and out-of-plane phonon modes, collectively facilitate asymmetry of heat transport.

## Validation of asymmetry of heat transport in real devices

To validate the out-of-plane asymmetry of heat transport effect, we fabricated a field-effect transistor (FET) device with a $MoS_2$/MoSSe/$WSe_2$ trilayer on top of two thin gold electrodes. Two heterostructures were prepared for comparison: one with forward stacking (Au/$MoS_2$/MoSSe/$WSe_2$ from bottom to top) and the other one with reverse stacking (Au/$WSe_2$/MoSSe/$MoS_2$ from bottom to top) (Fig. 5a–c). The thin gold electrode (1.5 μm × 30 μm, 100 nm thick) was used as a Joule heater. The surface temperature distribution of the device was measured by using a non-contact TTI method (Fig. 5e,f; Supplementary Fig. 6 provides more details). Also, 470-nm-wavelength light from a light-emitting diode was used as the incident light, which has the highest sensitivity to TMD materials. With the ×100 objective lens of the microscope subsystem, the TTI system could achieve a spatial resolution of approximately 260 nm. During the experiment, the heating power $P$ applied to the thin gold electrode was incrementally increased, and the average temperature rise $\Delta T$ was calculated within a rectangular area (1.5 μm × 30 μm) directly above the heating electrode. The results demonstrated that $\Delta T$ exhibited a favourable linear relationship with $P$, regardless of the stacking order of TMD materials (Fig. 5d), consistent with the theoretical predictions. Owing to the relatively lower out-of-plane thermal conductance, for a given heating power, the surface temperature of reverse-stacked heterostructure $\Delta T_{Rev}$ was lower than that of the forward-stacked heterostructure $\Delta T_{For}$. At a heating power of 58 mW, the difference $\Delta T_{For} - \Delta T_{Rev}$ reached 3.9 K. Through finite element analysis, we quantitatively determined that 90.5% of this temperature difference is attributable to the asymmetry in interfacial thermal conductance (Supplementary Section 1). This finding confirms the notable asymmetry of the heat transport effect of the trilayer heterostructure, consistent with the experimental results shown in Fig. 3. Considering the linear relationship between $\Delta T$ and $P$, the temperature difference $\Delta T_{For} - \Delta T_{Rev}$ became larger at a higher heating power. This confirmed that the multilayer heterostructure can be used as an intelligent thermal interfacial material. When the temperature of the core device reaches a high value, the heterostructure material on top facilitates rapid heat dissipation into the surroundings. Conversely, when the temperature of the core device is lower than that of the surroundings, the temperature gradient inverts and the thermal conductance decreases, protecting the core device from outside detrimental heat influx.

## Conclusions

We have reported the fabrication of a $MoS_2$/MoSSe/$WSe_2$ trilayer thermal Janus crystal that offers an asymmetric phonon transport property exceeding 90%. For chips containing multiple interfaces, integrations of this heterostructure could provide both rapid cooling and insulation from external high-temperature damage. The sub-5-nm thickness is also favourable for chip integration. When placed on top of a FET device, the heterostructure material generated a temperature difference of 3.9 K at the surface due to the asymmetric thermal transport effect. The variable stacking order and controllable interfacial twist angles of the heterostructure also offers flexibility for modulating moiré superlattices, interlayer coupling, SHC and band structures, which could potentially be used to achieve unidirectional thermal conduction.

## Methods

### Synthesis of $MoS_2$, $MoSe_2$, $WSe_2$ and Janus MoSSe monolayers

The fused silica and sapphire substrates purchased from Dongda Times, Chengdu Technology, were first pretreated with $O_2$ plasma. The metal precursors were predeposited on the fused silica piece by spin coating corresponding molten-salt aqueous solutions with optimized concentrations (12 mg $ml^{-1}$ of $Na_2MoO_4$, 18 mg $ml^{-1}$ of $Na_2MoO_4$ and 30 mg $ml^{-1}$ of $Na_2WO_4$ for the synthesis of $MoS_2$, $MoSe_2$ and $WSe_2$, respectively). Then, the precursor-coated pieces were heated at 80 °C for drying. The precursor-coated fused silica, sapphire substrate and chalcogenide crystal plate (ZnS or ZnSe) were stacked in a face-to-face manner by a customized holder. This integrated system was placed on a quartz plate and loaded in the chemical vapour deposition furnace, elevating to the optimized temperature for material growth (780 °C, 800 °C and 820 °C for the synthesis of $MoS_2$, $MoSe_2$ and $WSe_2$, respectively). The chamber pressure was kept at ~120 Pa with 100-s.c.c.m. Ar during the growth. After growth, the furnace was naturally cooled down to room temperature. The Janus MoSSe monolayer was fabricated by the post-processing of as-grown $MoS_2$ on $a$-plane sapphire substrate. The $MoS_2$ monolayers and ZnSe crystal plates were placed face to face and loaded into the chemical vapour deposition furnace. The Se substitution was carried out at 870 °C at low pressure with 120-s.c.c.m. Ar and 5-s.c.c.m. $H_2$. This high-temperature process was kept for 60 min to ensure the full substitution of the top-layer S atoms of $MoS_2$. The system was naturally cooled down to room temperature after substitution.

### Fabrication of X-shaped sensors and $MoS_2$/MoSSe/$WSe_2$ heterostructures

**Fabrication of the bottom sensor and electrode pad.** To achieve the required dimensional precision for the sensing device, electron-beam lithography was utilized to pattern the sensor and electrode pad with a resolution exceeding 10 nm. A 300-nm-thick layer of electron-beam (EB) resist (ZEP520A) was spin coated onto a silicon wafer coated with a 50-nm-thick $SiO_2$ layer, which was subsequently patterned into the bottom sensor and electrode pattern. Following this, a 50-nm-thick gold (Au) layer, preceded by an 8-nm-thick chromium adhesion layer, was deposited onto the patterned wafer via electron-beam PVD.

**Pretreatment of monolayer TMD samples for transfer.** The monolayer TMD samples, including $WSe_2$, $MoS_2$ and MoSSe, were initially synthesized on fused silica or sapphire substrates via the chemical vapour deposition method, as mentioned above. To reduce the adhesion force between the TMD material and substrate to facilitate subsequent transfer, the TMD samples were transferred to a clean $SiO_2$ substrate by using a typical PMMA method. First, a 300-nm-thick PMMA layer was spin coated on top of the TMD material. Then, the coated samples were immersed in a 10% sodium hydroxide solution for a duration of 1–3 h to etch the sapphire substrate and release the TMD/PMMA layer. After that, the samples were thoroughly rinsed with ultrapure water to remove chemical residuals. Finally, the TMD/PMMA layer was transferred onto a clean $SiO_2$ substrate, ready for the next transfer process.

**Transfer of monolayer TMD samples.** Subsequent to the pretreatment, we used the micromanipulation system (MicroSupport, AxisPro SS) to transfer a triangular single-crystalline $MoS_2$ domain to the $SiO_2$/Si substrate with pre-prepared bottom gold sensors and electrode. The position (1-μm accuracy) and orientation (0.3° precision) of each transferred $MoS_2$ crystal domain were meticulously adjusted by using two microprobes (TP-001) with a sharp tip of around 1 μm in diameter. After that, the substrate was heated to 135 °C and maintained at this temperature for 10 min on a temperature-controlled stage to enhance the adhesion force between the monolayer TMD and the substrate. Then, the sample was immersed in butanone at 45 °C for 30 min to fully dissolve the PMMA layer, thereby establishing an Au/$MoS_2$ stacking structure. To further remove possible chemical residues left by the dissolved PMMA, the sample was annealed at 400 °C for more than 8 h within a mixed atmosphere of hydrogen and argon under a slow flow rate. The good quality and cleanness of the crystalline structure can be ensured by the clear aberration-corrected TEM images of both cross-section (Fig. 1n) and moiré patterns (Fig. 1h–j). The same transfer process was repeated twice to transfer single-crystalline MoSSe and $WSe_2$ domains sequentially, forming a trilayer TMD heterostructure $MoS_2$/MoSSe/$WSe_2$ (the complete transfer process of the trilayer TMD sample is shown in Supplementary Video 1).

**Fabrication of top gold sensor and electrode pad.** After the transfer process in step (3), the same electron-beam lithography methodology delineated in step (1) was utilized to pattern the top gold sensor and electrode pad. Then, a 50-nm-thick Au layer was deposited by electron-beam PVD on the trilayer TMD sample to serve as the top sensor. The top and bottom sensors formed an X shape with the trilayer TMD sample in between, forming a stacked structure of Au/$MoS_2$/MoSSe/$WSe_2$/Au.

**Fabrication of the suspended structure.** After fabrication of the top sensor and electrode pad, a 300-nm-thick layer of EB resist was spin coated on the surface and patterned into a 5 μm × 5 μm square, whose centre coincided with the centre of the X-shaped sensors. Subsequently, the 50-nm-thick $SiO_2$ layer uncovered by EB resist was removed by using a reactive ion etching method with a $CHF_3$/Ar gas mixture. After that, the sample was put into a $XeF_2$ gas etching reactor for isotropic etching of the exposed Si substrate. The EB resist and top sensor protected the TMD sample from the etching gas. An etching depth of approximately 8 μm was sufficient to fully suspend the whole X-shaped sensors and 5 μm × 5 μm-wide sensing area, guaranteeing the highest measurement sensitivity for the interfacial thermal conductance of the trilayer TMD heterostructure.

**Removal of EB resist.** The chip was finally immersed in butanone at a temperature of 45 °C for 30 min to remove the EB resist layer on the surface. After that, the chip with suspended X-shaped sensors was dried by using a supercritical point drying system (Leica EM CPD300) to avoid surface-tension-induced damage to the sensors or TMD sample. On completion of these steps, the sensing device was ready to measure the out-of-plane thermal conductance of TMD heterostructures. The fabrication process was the same for the monolayer $MoS_2$ sample and bilayer $MoSe_2$/$WSe_2$ sample with suspended X-shaped sensors.

### Out-of-plane thermal conductance measurement method

The accurate measurement of out-of-plane thermal conductance necessitates the determination of both temperature gradient across the sample and the heat flux passing through it. In this study, two suspended gold nanosensors were used as individual precise resistance thermometers to quantify the temperature gradient. The resistance–temperature coefficient of the gold nanosensor was carefully calibrated beforehand. Utilizing a vacuum thermoelectric heating and cooling stage (INSTEC, TP102VF-MPS-6PB, ±0.001 K), the ambient temperature of the sample can be accurately controlled. By changing the electrical current applied to the X-shaped sensor, the corresponding data of the resistance and electrical power were acquired. A resistance–power curve was fitted to extrapolate the resistance of the sensor at zero current, which corresponds to the resistance at ambient temperature. Subsequently, by changing the ambient temperature of the stage, a resistance–temperature curve was constructed for each sensor.

In the current research, to measure the thermal conductance in the $J^+$ direction, the bottom gold nanosensor was subjected to a high current across its terminals, thereby functioning as a heater to generate Joule heating power $P$. A portion of this heat, quantified as $Q$, was conducted through the heterostructure in the out-of-plane direction to the other nanosensor on top. To quantify this thermal conduction process, a proportionality coefficient was defined as $\alpha$:

$$\alpha = \frac{Q}{P}. \tag{1}$$

Concurrently, a weak current was applied to the top sensor across terminals, serving as a detector. By monitoring the resistance change of the two sensors, their average temperature rises could be measured and the difference was denoted as $\Delta T_{\text{Average}}$. To determine the thermal conductance of the sample located in the centre of the two X-shaped sensors, it is necessary to calculate the temperature difference $\Delta T_{\text{Centre}}$ at the overlapping central area of both top and bottom sensors. The proportionality coefficient of these two temperature differences is denoted as $\beta$:

$$\beta = \frac{\Delta T_{\text{Centre}}}{\Delta T_{\text{Average}}}. \tag{2}$$

On the establishment of the above temperature difference and heat flux, the out-of-plane thermal conductance in the $J^+$ direction can be determined as follows:

$$G_{\text{eff}} = \frac{Q}{A\Delta T_{\text{Centre}}} = \frac{\alpha P}{\beta A \Delta T_{\text{Average}}}, \tag{3}$$

where $A$ represents the overlapping area between the two sensors (approximately 1 $\mu m^2$). $P$ can be accurately obtained by measuring the current and voltage applied to the heater sensor. $\Delta T_{\text{Average}}$ can be measured by assessing the resistances of both heater and detector sensors.

To obtain the proportionality coefficients $\alpha$ and $\beta$ in the above equations, a steady-state heat conduction simulation model was established in COMSOL Multiphysics. It is unambiguous that the shape of the electrode influences the coefficients $\alpha$ and $\beta$. Therefore, the geometric dimensions of sensor and electrode were precisely extracted from the scanning electron microscopy (SEM) images of suspended sensing device (Supplementary Fig. 4a) to establish the simulation model (Supplementary Fig. 4b,c). The thermal conductivities of gold sensor and silicon dioxide were measured and calibrated using the methods introduced in our previous work[33,41]. As a result, the out-of-plane thermal conductance $G_{\text{eff}}$ was the only unknown parameter to be determined. Both $\alpha$ and $\beta$ were uniquely influenced by $G_{\text{eff}}$, such that $\alpha = \alpha(G_{\text{eff}})$ and $\beta = \beta(G_{\text{eff}})$. Then, the aforementioned equation can be reformulated as follows:

$$\frac{P}{A\Delta T_{\text{Average}}} = \frac{\beta G_{\text{eff}}}{\alpha}. \tag{4}$$

Given the out-of-plane thermal conductance $G_{\text{eff}}$, the ratio $(\beta G_{\text{eff}})/\alpha$ can be calculated from the heat conduction simulation by COMSOL, allowing us to plot $G_{\text{eff}}$ versus $P/(A\Delta T_{\text{Average}})$ curve (Supplementary Fig. 4d). On the basis of this curve, the out-of-plane thermal conductance $G_{\text{eff}}$ can be solely determined from the corresponding value of $P/(A\Delta T_{\text{Average}})$ measured in the experiment.

### Molecular dynamics simulation

All molecular dynamics simulations were conducted using the LAMMPS software[42]. The intramolecular interactions within the TMD layer were described using a modified Stillinger–Weber potential[43], whereas the interlayer interactions between TMD molecules were modelled using the interlayer potential[44]. To simulate the interfacial thermal conductance, we first minimized the system's energy. The system was relaxed in an *NPT* ensemble at 300 K for 100 ps without external pressure to release residual stress. Subsequently, the system was further relaxed in an *NVE* ensemble for 100 ps to reach a stable state. Non-equilibrium molecular dynamics simulations were then performed for 5 ns, with the temperatures of the heat source and heat sink controlled by Langevin thermostats, where the damping parameter was set to 100 ps.

To calculate the vibrational DOS, we extracted the velocities of the two atomic layers closest to the interface. For the $WSe_2$/$MoSe_2$ heterojunction, these were the top Se atoms in $WSe_2$ and the bottom Se atoms in $MoSe_2$ (Supplementary Fig. 11a). The vibrational DOS was obtained by performing a fast Fourier transform on the velocity autocorrelation function, given by the following equation:

$$G(\omega) = \frac{1}{\sqrt{2\pi}} \int_0^{\tau_0} \frac{\langle v(0)v(t)\rangle}{\langle v(0)v(0)\rangle} \exp(i\omega t)\mathrm{d}t, \tag{5}$$

where $G(\omega)$ is the normalized vibrational DOS at frequency $\omega$, $v(t)$ is the atomic velocity at time $t$, $\tau_0$ is the integration time and the angle brackets denote ensemble averaging.

To calculate the spectral heat flux, we export the velocities and force vectors of all atoms every 10 fs. The force–velocity cross-correlation function is defined as follows:

$$K_{ji}(t_1 - t_2) = \frac{1}{2}\langle \mathbf{F}_{ji}(t_1) \cdot \mathbf{v}_j(t_2) - \mathbf{F}_{ij}(t_1) \cdot \mathbf{v}_i(t_2) \rangle. \quad (6)$$

The cross-correlation function is transformed into the frequency domain via Fourier transform:

$$\tilde{K}_{ji}(\omega) = \int_{-\infty}^{\infty} \mathrm{e}^{\mathrm{i}\omega t} K_{ji}(t) \mathrm{d}t. \quad (7)$$

The spectral heat flux is represented as

$$q_{i\to j}(\omega) = 2\mathrm{Re}[\tilde{K}_{ji}(\omega)]. \quad (8)$$

The total heat flux is represented as

$$Q_{i\to j} = \int_0^{\infty} \frac{1}{2\pi} q_{i\to j}(\omega) \mathrm{d}\omega. \quad (9)$$

By decomposing the force–velocity cross-correlation function into in-plane and out-of-plane components, we can determine the contributions of in-plane and out-of-plane vibrations to the heat flux:

$$Q_{\text{in plane}} = \frac{1}{2\pi}\int_0^{\infty} \mathrm{d}\omega\, \mathrm{Re}\left[\int_{-\infty}^{\infty} \mathrm{d}t\, \mathrm{e}^{\mathrm{i}\omega t}\langle \mathbf{F}_{ji,x}(t) \cdot \mathbf{v}_{j,x}(0) - \mathbf{F}_{ij,x}(t) \cdot \mathbf{v}_{i,x}(0) + \mathbf{F}_{ji,y}(t) \cdot \mathbf{v}_{j,y}(0) - \mathbf{F}_{ij,y}(t) \cdot \mathbf{v}_{i,y}(0)\rangle\right], \quad (10)$$

$$Q_{\text{out of plane}} = \frac{1}{2\pi}\int_0^{\infty} \mathrm{d}\omega \mathrm{Re}\left[\int_{-\infty}^{\infty} \mathrm{d}t\, \mathrm{e}^{\mathrm{i}\omega t}\langle \mathbf{F}_{ji,z}(t) \cdot \mathbf{v}_{j,z}(0) - \mathbf{F}_{ij,z}(t) \cdot \mathbf{v}_{i,z}(0)\rangle\right]. \quad (11)$$

## Data availability

The data supporting the findings of this study are available from the corresponding authors upon reasonable request. Source data are provided with this paper.

## References


1. Huang, X. et al. A graphite thermal Tesla valve driven by hydrodynamic phonon transport. *Nature* **634**, 1086–1090 (2024).
2. Wang, H. et al. Experimental study of thermal rectification in suspended monolayer graphene. *Nat. Commun.* **8**, 15843 (2017).
3. Ju, R. et al. Nonreciprocal heat circulation metadevices. *Adv. Mater.* **36**, 2309835 (2024).
4. Lei, M. et al. Reconfigurable, zero-energy, and wide-temperature loss-assisted thermal nonreciprocal metamaterials. *Proc. Natl Acad. Sci. USA* **121**, e2410041121 (2024).
5. Li, Y. et al. Transforming heat transfer with thermal metamaterials and devices. *Nat. Rev. Mater.* **6**, 488–507 (2021).
6. Yagmurcukardes, M. et al. Quantum properties and applications of 2D Janus crystals and their superlattices. *Appl. Phys. Rev.* **7**, 011311 (2020).
7. Walther, A. & Müller, A. H. E. Janus particles: synthesis, self-assembly, physical properties, and applications. *Chem. Rev.* **113**, 5194–5261 (2013).
8. Huang, M. et al. Selective assemblies of giant tetrahedra via precisely controlled positional interactions. *Science* **348**, 424–428 (2015).
9. Yan, J. et al. Linking synchronization to self-assembly using magnetic Janus colloids. *Nature* **491**, 578–581 (2012).
10. Song, S. et al. Janus graphene nanoribbons with localized states on a single zigzag edge. *Nature* **637**, 580–586 (2025).
11. Hu, T. et al. Intrinsic and anisotropic Rashba spin splitting in Janus transition-metal dichalcogenide monolayers. *Phys. Rev. B* **97**, 235404 (2018).
12. Wang, J. et al. Even-integer quantum Hall effect in an oxide caused by a hidden Rashba effect. *Nat. Nanotechnol.* **19**, 1452–1459 (2024).
13. Guo, H., Zhang, X. & Lu, G. Tuning moiré excitons in Janus heterobilayers for high-temperature Bose-Einstein condensation. *Sci. Adv.* **8**, eabp9757 (2022).
14. Lu, A.-Y. et al. Janus monolayers of transition metal dichalcogenides. *Nat. Nanotechnol.* **12**, 744–749 (2017).
15. Shi, J. et al. Giant room-temperature nonlinearities in a monolayer Janus topological semiconductor. *Nat. Commun.* **14**, 4953 (2023).
16. Liu, C. et al. Anomalous photovoltaics in Janus MoSSe monolayers. *Nat. Commun.* **16**, 544 (2025).
17. Yankowitz, M. et al. Tuning superconductivity in twisted bilayer graphene. *Science* **363**, 1059–1064 (2019).
18. Sharpe, A. L. et al. Emergent ferromagnetism near three-quarters filling in twisted bilayer graphene. *Science* **365**, 605–608 (2019).
19. Serlin, M. et al. Intrinsic quantized anomalous Hall effect in a moiré heterostructure. *Science* **367**, 900–903 (2020).
20. Cao, Y. et al. Unconventional superconductivity in magic-angle graphene superlattices. *Nature* **556**, 43–50 (2018).
21. Cao, Y. et al. Correlated insulator behaviour at half-filling in magic-angle graphene superlattices. *Nature* **556**, 80–84 (2018).
22. Oh, M. et al. Evidence for unconventional superconductivity in twisted bilayer graphene. *Nature* **600**, 240–245 (2021).
23. Chen, G. et al. Signatures of tunable superconductivity in a trilayer graphene moiré superlattice. *Nature* **572**, 215–219 (2019).
24. Lu, X. et al. Superconductors, orbital magnets and correlated states in magic-angle bilayer graphene. *Nature* **574**, 653–657 (2019).
25. Chen, G. et al. Tunable correlated Chern insulator and ferromagnetism in a moiré superlattice. *Nature* **579**, 56–61 (2020).
26. Cai, J. et al. Signatures of fractional quantum anomalous Hall states in twisted $MoTe_2$. *Nature* **622**, 63–68 (2023).
27. Liu, K. et al. Evolution of interlayer coupling in twisted molybdenum disulfide bilayers. *Nat. Commun.* **5**, 4966 (2014).
28. Zhang, L. et al. Effect of twist angle on interfacial thermal transport in two-dimensional bilayers. *Nano Lett.* **23**, 7790–7796 (2023).
29. Zhang, J. et al. Janus monolayer transition-metal dichalcogenides. *ACS Nano* **11**, 8192–8198 (2017).
30. Li, H. et al. From bulk to monolayer $MoS_2$: evolution of raman scattering. *Adv. Funct. Mater.* **22**, 1385–1390 (2012).
31. Li, Z. et al. Temperature-dependent Raman spectroscopy studies of 1–5-layer $WSe_2$. *Nano Res.* **13**, 591–595 (2020).
32. Soubelet, P. et al. Resonance effects in the Raman scattering of monolayer and few-layer $MoSe_2$. *Phys. Rev. B* **93**, 155407 (2016).
33. Zhang, Y. et al. Simultaneous electrical and thermal rectification in a monolayer lateral heterojunction. *Science* **378**, 169–175 (2022).
34. Ashcroft, N. W., Mermin, N. D. & Rodriguez, S. Solid state physics. *Am. J. Phys.* **46**, 116–117 (1978).
35. Yasaei, P. et al. Interfacial thermal transport in monolayer $MoS_2$- and graphene-based devices. *Adv. Mater. Interfaces* **4**, 1700334 (2017).
36. Freedy, K. M. et al. Titanium contacts to $MoS_2$ with interfacial oxide: Interface chemistry and thermal transport. *Phys. Rev. Mater.* **3**, 104001 (2019).

37. Liu, J., Choi, G.-M. & Cahill, D. G. Measurement of the anisotropic thermal conductivity of molybdenum disulfide by the time-resolved magneto-optic Kerr effect. *J. Appl. Phys.* **116**, 233107 (2014).
38. Brown, D. B., Shen, W., Li, X., Xiao, K., Geohegan, D. B. & Kumar, S. Spatial mapping of thermal boundary conductance at metal–molybdenum diselenide interfaces. *ACS Appl. Mater. Interfaces* **11**, 14418–14426 (2019).
39. Kim, S. E. et al. Extremely anisotropic van der Waals thermal conductors. *Nature* **597**, 660–665 (2021).
40. Xu, B. et al. Heat conduction modulation in incommensurate twisted stacking of transition-metal dichalcogenide. *Adv. Funct. Mater.* **35**, 2422761 (2025).
41. Zhang, Q. G., Cao, B. Y., Zhang, X., Fujii, M. & Takahashi, K. Influence of grain boundary scattering on the electrical and thermal conductivities of polycrystalline gold nanofilms. *Phys. Rev. B* **74**, 134109 (2006).
42. Thompson, A. P. et al. LAMMPS—a flexible simulation tool for particle-based materials modeling at the atomic, meso, and continuum scales. *Comput. Phys. Commun.* **271**, 108171 (2022).
43. Jiang, J.-W. Misfit strain-induced buckling for transition-metal dichalcogenide lateral heterostructures: a molecular dynamics study. *Acta Mech. Solida Sin.* **32**, 17–28 (2019).
44. Jiang, W. et al. Anisotropic interlayer force field for group-VI transition metal dichalcogenides. *J. Phys. Chem. A* **127**, 9820–9830 (2023).

## Acknowledgements

This work was supported by the National Key Research and Development Program of China (grant number 2023YFB4404100 to H.W.) and the National Natural Science Foundation of China (grant numbers 52425601 to B.C., 52327809 to B.C., 52276072 to H.W., 92577201 to K.L. and 12427806 to K.L.).

## Author contributions

H.W., K.L. and B.C. supervised the project. G.X. grew the MoSSe materials and performed the polarization-resolved SHG characterization. Q.G. performed the TEM characterization. H.Z. and H.W. designed and fabricated the X-shaped sensing device, prepared the three-layer heterojunction samples, and performed the electrical and thermal property measurements and data analysis. H.Z. performed the Raman spectroscopy mapping and finite element simulations. H.Y. performed the molecular dynamics simulations and wrote the discussion. H.W. fabricated the FETs and Z.L. characterized them using the TTI system. H.Z., H.W., H.Y. and Z.L. wrote the manuscript with the participation of all authors. All authors participated in the discussion of the results and in the revision of the manuscript.

## Competing interests

The authors declare no competing interests.

## Additional information

**Supplementary information** The online version contains supplementary material available at https://doi.org/10.1038/s41928-026-01620-5.

**Correspondence and requests for materials** should be addressed to Haidong Wang, Kaihui Liu or Bingyang Cao.

**Peer review information** *Nature Electronics* thanks Zlatan Aksamija, Cheng-Wei Qiu and the other, anonymous, reviewer(s) for their contribution to the peer review of this work.